FULL PAPER

Flexible Conducting Panels

ADVANCED
FUNCTIONAL
MATERIALS

www.afm-journal.de

Highly Stable Ni-Based Flexible Transparent Conducting Panels Fabricated by Laser Digital Patterning

Vu Binh Nam, Jaeho Shin, Yeosang Yoon, Trinh Thi Giang, Jinhyeong Kwon, Young D. Suh, Junyeob Yeo, Sukjoon Hong, Seung Hwan Ko,* and Daeho Lee*

A novel simple laser digital patterning process to fabricate Ni-based flexible transparent conducting panels using solution-processed nonstoichiometric nickel oxide (NiO$_x$) thin films and their applications for flexible transparent devices are reported in this study. A large-scale synthesis route to produce NiO$_x$ nanoparticle (NP) ink is also demonstrated. A low-power continuous-wave laser irradiation photothermochemically reduces and sinters selected areas of a NiO$_x$ NP thin film to produce Ni electrode patterns. Owing to the innovative NiO$_x$ NP ink and substantially lowered applied laser power density, Ni conductors can be fabricated, for the first time to the best of the authors' knowledge, even on a polyethylene terephthalate substrate, which is known to have one of the lowest glass-transition temperatures among polymers. The resultant Ni electrodes exhibit a high-temperature oxidation resistance up to approximately 400 °C, and high corrosion resistance in tap water and even in seawater. Moreover, a superior mechanical stability of the Ni conductors is confirmed by tape-pull, ultrasonic-bath, bending/twisting, and cyclic bending (up to 10 000 cycles) tests. Finally, flexible transparent touch screen panels and electrical heaters are fabricated with mesh-type Ni conductors to demonstrate possible applications.

1. Introduction

Transparent conducting electrodes (TCEs)[1] are essential components of various optoelectronic devices such as thin-film displays, solar cells, transparent heating components, and touch screens. In the current transparent conductor industry, indium tin oxide (ITO) films coated on glass prevails in the market. However, ITO suffers from several limitations such as brittleness and lack of flexibility of ITO layers, and costly deposition method requiring vacuum-based equipment, which hinders its application to the next-generation electronics, particularly to flexible or stretchable electronics. Therefore, the demand for alternative materials and deposition methods of TCEs is rapidly increasing. Among alternatives to conventional deposition or patterning methods for conducting/semiconducting electrodes, a laser digital patterning process on solution-processed nanoparticle (NP) thin films[2] has recently attracted significant attention since it enables to achieve a photolithography-free, low-cost, and on-demand electrode fabrication. The laser digital patterning process, in particular, can be applied to fabricate flexible electronic devices owing to lowered thermal stress exerting on thermally vulnerable polymer substrates (see expanded discussion in Section S1, Supporting Information). As materials for laser digital patterning in the early stage, NPs or nanocomposites composed of noble metals such as Ag or Au have been widely employed[3] because these nanomaterials are oxidation resistant, and thus can be easily formed to conducting electrodes simply by sintering. However, nowadays, there is an increasing demand to diversify the electrode materials not only owing to the high price of the noble metals but also particularly owing to the need for unique properties of relevant

V. B. Nam, T. T. Giang, Prof. D. Lee
Laser and Thermal Engineering Lab
Department of Mechanical Engineering
Gachon University
1342 Seongnamdaero, Sujeong-gu, Seongnam
Gyeonggi 13120, South Korea
E-mail: dhl@gachon.ac.kr
J. Shin, Y. Yoon, Dr. J. Kwon, Dr. Y. D. Suh, Prof. S. H. Ko
Applied Nano and Thermal Science Lab
Department of Mechanical Engineering
Seoul National University
1 Gwanak-ro, Gwanak-gu, Seoul 08826, South Korea
E-mail: maxko@snu.ac.kr

Prof. S. H. Ko
Institute of Engineering Research/Institute of Advanced Machinery
and Design (SNU-IAMD)
Seoul National University
1 Gwanak-ro, Gwanak-gu, Seoul 08826, South Korea
Prof. J. Yeo
Novel Applied Nano Optics Lab
Department of Physics
Kyungpook National University
80 Daehak-ro, Pook-gu, Daegu 41566, South Korea
Prof. S. Hong
Department of Mechanical Engineering
Hanyang University
55 Hanyangdaehak-ro, Sangnok-gu, Ansan 15588, South Korea

materials. However, common metals, in general, are very easily oxidized at the nanoscale. Therefore, these NPs need to undergo sintering and reduction simultaneously, referred to as reductive sintering, to form conducting metal electrodes. Laser-induced reductive sintering (LRS) of metal oxide NPs or nanowires has previously been demonstrated to produce Cu electrodes, which is facilitated by the thermal instabilities of oxides and reducing agents in the nanomaterial ink.[4] Cu is an attractive material as a conductor owing to their high intrinsic conductivity and low price, however, in many circumstances, electrodes should function more stably under various stimulations such as chemicals, high temperature, and humidity.

Ni possesses a high corrosion resistance and a silver-like color, and thus is suitable for use as conductors in electronic devices, current collectors or catalysts in electrochemical devices,[5] composite materials,[1b] and plating metals.[6] Moreover, Ni has possible applications for magnetically modulated devices and bio-devices owing to its characteristic magnetic properties.[7] However, there are only few reports on solution-processable Ni electrode deposition through the LRS process and its applications. Lee et al.[8] reported for the first time a fast and simple Ni electrode patterning method by applying the LRS process on solution-processed nonstoichiometric nickel oxide (NiO_x) thin films. Rho et al.[9] successfully combined inkjet printing and the LRS process to produce highly crystalline Ni/NiO hybrid electrodes. However, the LRS process on NiO_x NP films in the previous studies[8,9] has several limitations. First, the LRS process for flexible Ni conductors was successful only on a polyimide (PI) substrate that has high temperature endurance, but has a low transmittance, because a relatively high temperature needs to be induced for reductive sintering of the utilized NiO_x NPs. Second, the synthesis method of the NP ink is not adequate for mass production due to the relatively low recovery rate of NPs from the precursor solution. Lastly, the employed chemicals, such as toluene and oleylamine, are not easy to handle. Therefore, it is required to develop an alternative synthesis method for the material, and a corresponding LRS process to fabricate Ni patterns on low-melting-point polymers to expand the functionality of the resultant electrodes.

In this study, we introduce a simple laser digital patterning process to fabricate Ni-based flexible transparent conducting panels using solution-processed NiO_x thin films, as well as a large-scale synthesis route to produce NiO_x NP ink. High-resolution, highly conductive, and customized Ni electrode patterns can be generated by the LRS process using a continuous-wave (CW) laser under ambient conditions. Owing to the low required temperature for the reductive sintering of the reformulated NiO_x NPs, Ni electrode patterning is successful even on polyethylene terephthalate (PET), which has a very low glass-transition temperature, yet is highly transparent. The optical transmittance and electrical conductance of panels composed of Ni grids can be easily adjusted by varying the pattern designs in the integrated computer-aided design (CAD) system. Superior mechanical and electrical properties and excellent durability of the Ni electrodes are confirmed by various performance tests. Furthermore, the high thermal stability against oxidation up to approximately 400 °C and high corrosion resistance in tap water and seawater of the Ni electrodes are also verified. Flexible transparent touch screen panels and high-temperature flexible transparent heaters are demonstrated as practical applications.

2. Results and Discussion

We developed a large-scale synthesis route to produce a high-concentration well-dispersed NiO_x NP composite ink comprising NiO_x NPs and additive polymers dispersed in a solvent (details are provided in the Experimental Section). 1-Pentanol was selected as the NP ink solvent because it has adequate viscosity and vapor pressure to produce thin films with a suitable thickness by spin-coating; in addition, it completely dissolves PVP and cetyltrimethylammonium bromide (CTAB). PVP functions as both a dispersant and reducing agent. The addition of a small amount of CTAB enhances the stability of dispersion of the NP ink, thus yielding better qualities of the resultant NiO_x thin films and Ni electrodes. The NPs remain well dispersed even at a high concentration in the ink. We successfully demonstrated the synthesis of 273 g dry weight of NiO_x NPs, which can produce approximately 750 mL of NiO_x NP composite ink (NiO_x NP content in the ink: >30 wt%). The produced $Ni(OH)_2$, NiO_x NPs, and NiO_x NP composite ink are shown in **Figure 1**a,b. The diameters of the synthesized NiO_x NPs are in the range of 4–8 nm, verified by transmission electron microscopy (TEM), as shown in Figure 1c. The particle size distribution is displayed in Figure S2 in the Supporting Information. The high-resolution TEM (HRTEM) image and selected-area electron diffraction (SAED) pattern in Figure 1d,e, respectively, confirm that the NPs have a well-defined cubic crystalline structure, with clear lattice fringes; the spacing between two adjacent fringes is 0.24 nm, corresponding to the (111) plane of NiO_x. NiO_x films can be easily formed on both soda-lime glass and PET substrates by a simple spin-coating technique. The thickness of the film can be easily controlled depending on the purpose by varying the ink concentration or spin-coating process parameters. For example, thicker films are advantageous for a higher conductivity, while thinner films are advantageous for a higher transmittance (see expanded discussion in Section S3, Supporting Information). In this study, the concentration of NiO_x NPs in the solvent and spin-coating speed were 31 wt% and 1000 rpm, respectively, for both glass and PET substrates. Owing to the well-dispersed NP ink, the spin-coated NiO_x film has a smooth and uniform surface, as shown in Figure 1f. We verified that the NiO_x film can also be deposited by a bar-coating method, which can be applied to a larger substrate. It is worth noting that the entire process was performed under ambient conditions.

The subsequent LRS process was applied on the as-prepared NiO_x film using a 532 nm CW Nd:YVO_4 laser. A schematic of the laser setup for the LRS process is shown in Figure 1g. The spot diameter of the focused laser beam through a telecentric lens of the galvanometer scanner was approximately 25 µm. The CAD system integrated with the scanner enables digital patterning of customized shapes on the NiO_x thin film. In order to reveal optimized laser process parameters, the scanning speed was fixed at 50 mm s^{-1}, while the applied laser power was carefully controlled. The optimal laser power depends on the thermal properties of the substrate owing to the heat transfer mechanism, as described below. Upon laser irradiation, the NiO_x NPs are reduced to Ni NPs, and then are sintered to form electrodes. After the LRS process, the unsintered parts of the film can be easily removed by rinsing with water or suitable organic solvents, while the sintered parts remain intact with excellent adhesion to the substrate. The excellent adhesion
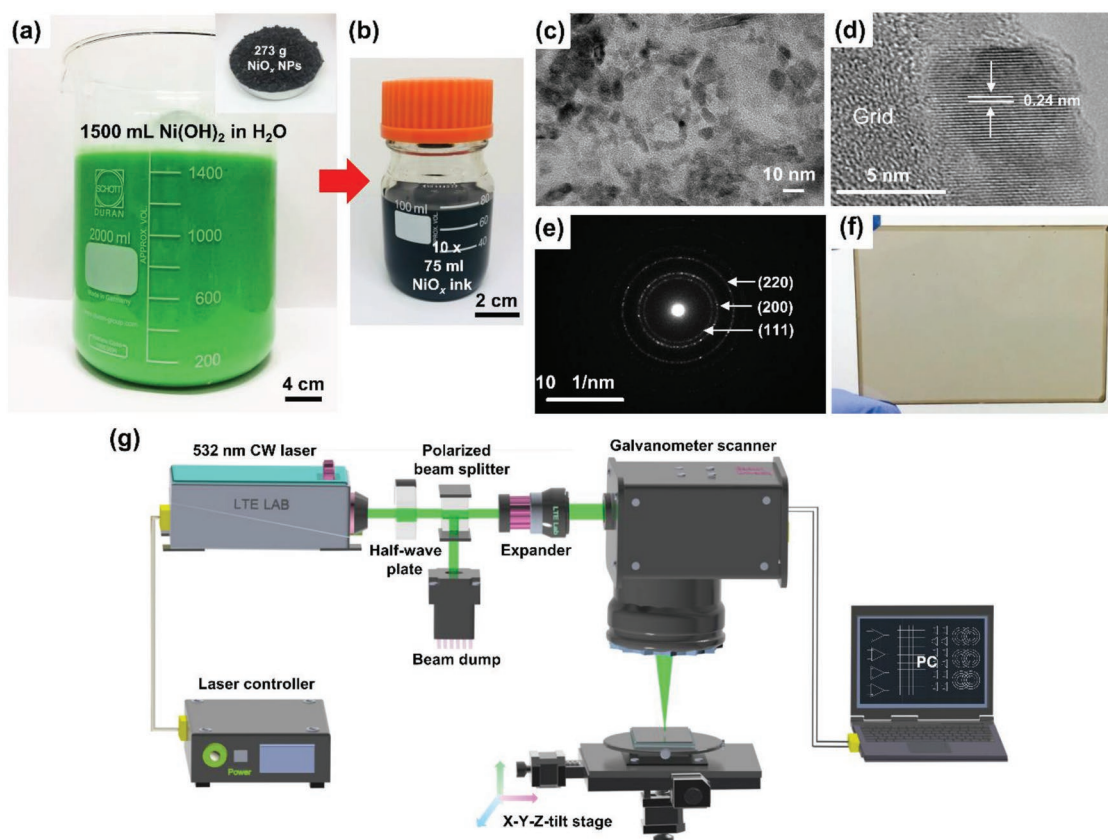
ADVANCED
SCIENCE NEWS
www.advancedsciencenews.com

ADVANCED
FUNCTIONAL
MATERIALS
www.afm-journal.de

Figure 1. a) Photograph of the Ni(OH)$_2$ colloidal solution before calcination at 270 °C. The inset shows 273 g of NiO$_x$ NPs after calcination at 270 °C for 2 h. b) Photograph of 75 mL of NiO$_x$ ink containing NiO$_x$ NPs, PVP, CTAB, and 1-pentanol. c) TEM image of the synthesized NiO$_x$ NPs. d) High-resolution TEM image of the synthesized NiO$_x$ NPs. e) SAED pattern from the synthesized NiO$_x$ NPs. f) Spin-coated NiO$_x$ film on a 7.6 cm × 5.2 cm glass substrate. g) Schematic illustration of the LRS setup.

between the LRS-processed Ni electrode and the substrate could be attributed to laser-induced localized melting and subsequent solidification of the electrode–substrate interface. Detailed discussion is provided in Section S4, Supporting Information.

The surface morphology of the Ni electrodes on a glass substrate is analyzed using scanning electron microscopy (SEM) and atomic force microscopy (AFM). **Figure 2**a,b shows SEM images of mesh-type electrodes defined by single scan of the laser beam at a power of 50 mW on the glass substrate. The measured width of each line is approximately 35 μm, which is larger than the laser-beam spot size, because of heat diffusion on the film induced by the laser irradiation. The reduction of NiO$_x$ to Ni upon the laser irradiation is confirmed by the elemental mapping images of Ni and O acquired using energy-dispersive X-ray spectroscopy (EDS), as shown in the insets of Figure 2a. The images show a clear contrast between Ni and O elements in the electrodes, suggesting that the laser irradiation effectively reduces the NiO$_x$ NPs to form Ni electrodes, while washing process cleanly removes the nonirradiated parts. It is worth noting that the oxygen elements detected in the background are partly from the glass substrate. The surface morphology and chemical components of the electrode can vary depending on the position, owing to the Gaussian profile of the laser beam, as shown in Figure 2c. The Ni ratio at the edge of the electrode is lower than that at the center of the electrode, which leads to

a reduced conductivity of the electrodes. Application of a flat top beam profile for example, may mitigate this type of nonuniformity of the chemical composition. X-ray diffraction (XRD) analysis for the NiO$_x$ film NP film before and after the LRS process (Figure S5, Supporting Information) also verifies that the NiO$_x$ having a face-centered cubic (FCC) crystal structure is reduced and sintered to metallic Ni having an FCC crystal structure (see expanded discussion in Section S5, Supporting Information).

The reduction mechanism of the nonstoichiometric NiO$_x$ NPs in the solution composed of PVP, CTAB, and 1-pentanol by laser irradiation has not been yet fully revealed; however, it can be inferred from the previously reported studies on the reduction of a CuO NP thin film which includes PVP. Kim and co-workers[10] explained that an intense pulsed light irradiation decomposed PVP to generate carboxylic acid, which served as a reducing agent to reduce the CuO NPs to Cu NPs. Woo et al.[11] investigated the reduction effect of various carboxylic acids on CuO NP films. Yang and co-workers[4a,12] explained the role of PVP and carboxylic acid as a reducing agent for CuO NPs during the laser irradiation process; they also claimed that the solvent of the NP ink is related to the reduction reaction. In order to verify whether the solvent is essential for the reduction reaction in our case, we performed LRS on a completely dried NiO$_x$ NP thin film baked at 120 °C for 5 min after spin-coating, and observed that identical results were achieved at the same laser processing parameters,
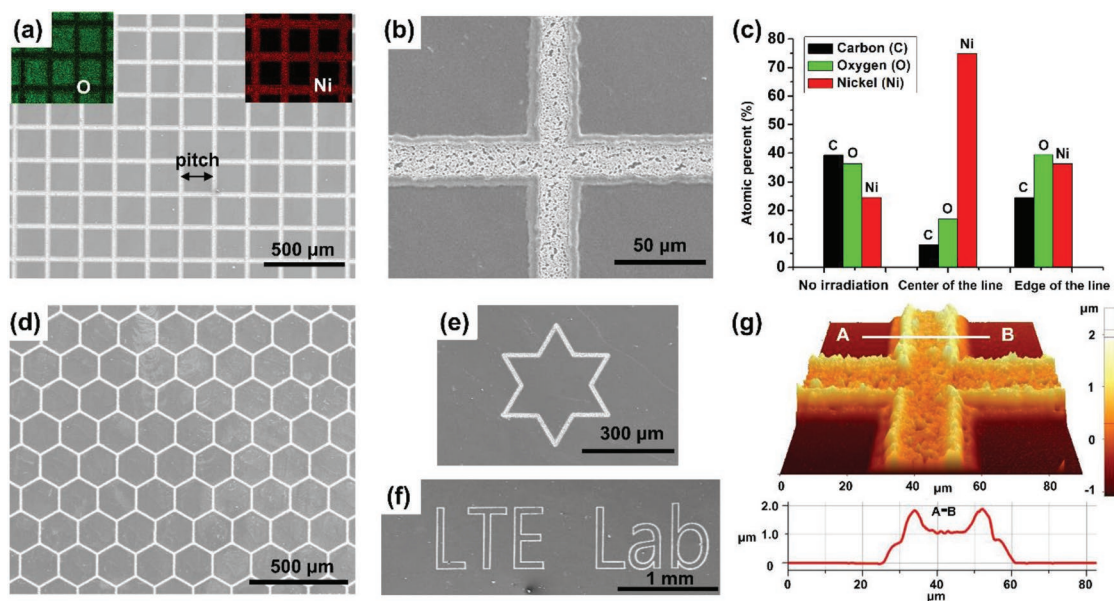
Figure 2. a) Top-view SEM image of mesh-type electrodes on the glass substrate. The insets show elemental mapping images for O and Ni of the electrodes. b) SEM image showing a magnified view of the Ni electrodes in a); the line width is approximately 35 µm. c) Comparison of the chemical compositions before (left columns) and after the laser irradiation at the center (middle columns) and edge (right columns) of the electrode. d–f) Customized electrode patterns obtained by the LRS process through the change of CAD data. g) AFM image of the Ni electrodes.

which confirms that the solvent is not an essential component for reduction. We also verified that laser irradiation cannot induce reduction of NiO_x NPs without PVP addition in the ink. Considering these results, we propose the LRS mechanism of NiO_x NPs as follows: under the laser irradiation, PVP in the NP thin film thermally decomposes to generate carboxylic acid, which reduces NiO_x NPs to Ni NPs. The reduced Ni NPs then sinter together to form continuous electrodes. It is worth noting that LRS of the NiO_x NP film under ambient conditions occurs in a certain range of laser parameters. An insufficient laser power or excessive laser scanning speed, out of the optimum level, fails to reduce the NiO_x NP film as PVP does not decompose. On the contrary, an excessive laser power or insufficient laser scanning speed reoxidizes the electrodes and can destroy the electrode surface or damage the substrate in an extreme case. Figure 2d–f shows various metal patterns on glass substrates fabricated by LRS at the laser power of 50 mW. Considering that the laser beam diameter is approximately 25 µm, the laser power density is approximately 10 kW cm^{-2}, an order of magnitude smaller than that in the previous study using different NiO_x NP ink.[8b] The electrode patterns can be easily adjusted by changing the CAD data. The nominal thickness of the electrode measured by AFM is approximately 1.2 µm, as shown in Figure 2g. The thicker edges are attributed to thermocapillarity. It is worth noting that the axes of Figure 2g have different scales. The root-mean-square (RMS) value of the surface roughness around the center area of the electrode is 6.21 nm. The lowest resistivity of the Ni conductor after the reductive sintering with the optimized laser power (for a glass substrate) is approximately 989 nΩ m, which was calculated by $\rho = R(A/l)$, where R, A, and l are the resistance, cross section, and length of a single electrode line, respectively. The resistivity is approximately 14 times higher than that of bulk Ni (69.3 nΩ m at room temperature), possibly owing to nanopores

generated in the conductor, partial reoxidation, and incomplete reduction, but still sufficiently low for use in various applications as electrical conductors.

One of the distinct features of Ni electrodes over other metal electrodes is their antioxidation and corrosion-resistant properties. After fabrication of Ni electrode by the LRS process, the high-temperature oxidation resistance of the Ni electrode was evaluated by heating the sample in air. The electrical resistance of the Ni electrode on a glass substrate was recorded after maintaining the electrode at each elevated temperature for 5 min and cooling down to room temperature. As shown in **Figure 3**a, the electrode restores its original resistance (R_o) with a variation smaller than 9% after heating up to 350 °C. Even after heating to 400 °C, the increase in resistance is limited to 60%. However, the resistance begins to significantly increase from 420 °C, and is not measurable above 440 °C indicating that the electrode is fully oxidized. The anticorrosion test of the Ni electrode was performed by immersing the samples in tap water or seawater. As shown in Figure 3b, the resistance variation of the electrode after a 9 d immersion in both environments is smaller than 10%. To compare anticorrosion behavior, Cu electrodes were fabricated in a similar way as Ni by the LRS process. Details of the CuO_x NP synthesis are provided in the Experimental Section. In contrast to Ni, the Cu electrode was quickly oxidized after 2 h and 8 d immersions in seawater and tap water, respectively. In addition, the resistance of the Ni electrodes was not changed in a period of more than 5 months under ambient conditions. The detail of the origin of the superior chemical and mechanical performances of the LRS-processed Ni electrodes is discussed in Section S6 in the Supporting Information. As the adhesion of the electrode on the substrate is an important issue, we performed a tape-pull test several times using a conventional 3M tape, and verified that the Ni electrode did not detach from the glass substrate.
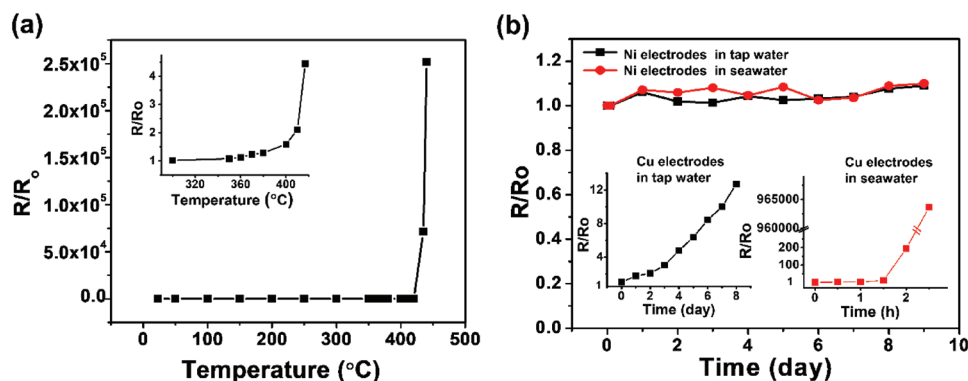
Figure 3. a) Relative resistance variation (R/R_o) with the increase in the temperature, from room temperature to 440 °C. The inset shows a magnified view in the range of 300–420 °C. b) Measured R/R_o of the Ni electrodes in tap water and seawater. The insets show the measured R/R_o of the Cu electrodes in tap water (left) and seawater (right).

As a harsher test, an ultrasonication test was performed. The Ni electrodes were intact even after dipping in an ultrasonic bath over 1 min. The detail of adhesion test is discussed in Section S7 in the Supporting Information with video clips provided as Movies S1 and S2 in the Supporting Information.

Recently, Ag[3a,13] and Cu[14] grids have emerged as next-generation flexible transparent conductors owing to their high conductivities, high transmittances, and low processing temperatures. In the recent study,[8b] Ni electrode grids on a glass substrate were demonstrated as a transparent conducting panel for touch screen application. However, the Ni electrode grids failed to concurrently satisfy transparency and flexibility since PI is the only applicable flexible substrate, as mentioned above. On the other hand, as the newly synthesized NiO_x NP ink in this study can be reduced and sintered with a lower laser power owing to the different reduction mechanism (see expanded discussion in Section S8, Supporting Information), Ni electrode patterns can be deposited on a PET substrate, which is highly transparent and flexible, yet has a very low glass-transition temperature (T_g −80 °C). Transparent conducting panels are fabricated with mesh-type Ni electrodes. The balance between transmittance (T) and sheet resistance (R_s) can be adjusted by altering the pitch of the mesh patterns. **Figure 4**a shows the sheet resistance as a function of the grid pitch. The sheet resistance was calculated by: $R_s = (R \cdot w)/l$, where R, w, and l are the resistance, width, and length of the mesh-type Ni panel, respectively. The resistance was measured by the two-terminal method with conductive silver paste applied on the two sides of each 1 cm × 1 cm mesh pattern. The R_s increases almost linearly with the pitch. For example, the R_s for the Ni meshes with pitches of 500, 300, and 80 µm on PET are 96, 53, and 14 Ω sq^{-1}, respectively. Figure 4b shows a 3 cm × 3 cm flexible transparent conducting panel on PET composed of mesh-type Ni electrodes with a pitch of 500 µm; no damage of the electrode layer on PET is observed after the LRS process (inset of Figure 4b). The total laser processing time required for scanning a 3 cm × 3 cm area with a scan speed of 50 mm s^{-1} is only approximately 2 min, which can be possibly shortened by further optimization. It is worth noting that the lowest R_s values reached on both glass and PET substrates with each optimized laser parameters do not differ within experimental error. The substrate-based optical transmittance of the Ni flexible mesh-type conductors

is plotted as a function of the grid pitch (Figure 4c) and R_s (Figure 4d). R_s smaller than 100 Ω sq^{-1} with a transmittance as high as 90% can be achieved. By utilizing the CAD system integration, customized digital electrode patterns with a larger line width can be obtained by changing the drawing design, as shown in Figure 4e. It is worth to note that we employed the galvanometer scanner because it is advantageous for fast and stable scanning with a simple setup, and enables easy control of arbitrary pattern designs. However, the suggested LRS process method in this work can fabricate electrodes invisible to naked eyes (line width <5 µm) as long as we change the optical system (see expanded discussion in Section S9, Supporting Information).

The optimized laser power for LRS on PET at a scanning speed of 50 mm s^{-1} was approximately 20 mW, significantly lower than that in the case of the glass substrate. The different laser power requirements depending on the substrate material can be explained by the following equation,[15]

$$\Delta T(x,t) = \frac{2q_0''(\alpha t/\pi)^{1/2}}{k} \exp\left(\frac{-x^2}{4\alpha t}\right) - \frac{q_0''x}{k} erfc\left(\frac{x}{2\sqrt{\alpha t}}\right) \quad (1)$$

from the basic theory of transient diffusive heat transfer in a semi-infinite solid upon a constant heat flux input (q''_0), where ΔT, x, t, α, and k correspond to temperature increase, depth from the surface, time, thermal diffusivity, and thermal conductivity of the substrate, respectively. Assuming the thickness of the NP film is very small compared with that of the substrate, the induced surface ($x = 0$) temperature increase is proportional to the value of $\alpha^{0.5}k^{-1}$. As indicated in **Table 1**, the $\alpha^{0.5}k^{-1}$ value of PET is 2.94 times higher than that of soda-lime glass, which is in reasonable agreement with the ratio of the required laser powers of 20 and 50 mW for PET and glass, respectively.

In order to evaluate the mechanical flexibility and electrical reliability of the Ni electrodes on PET, resistance change was measured under various mechanical deformation conditions. A 2.5 cm × 4.5 cm mesh-type Ni conductor pad on PET was fabricated; subsequently, copper tapes were attached to the ends of the two sides. **Figure 5**a shows the change in relative resistance of the pad at various bending radii. The convex and the concave bending apply tension and compression to the electrodes on the curved surfaces, respectively. In the concave mode, the resistance
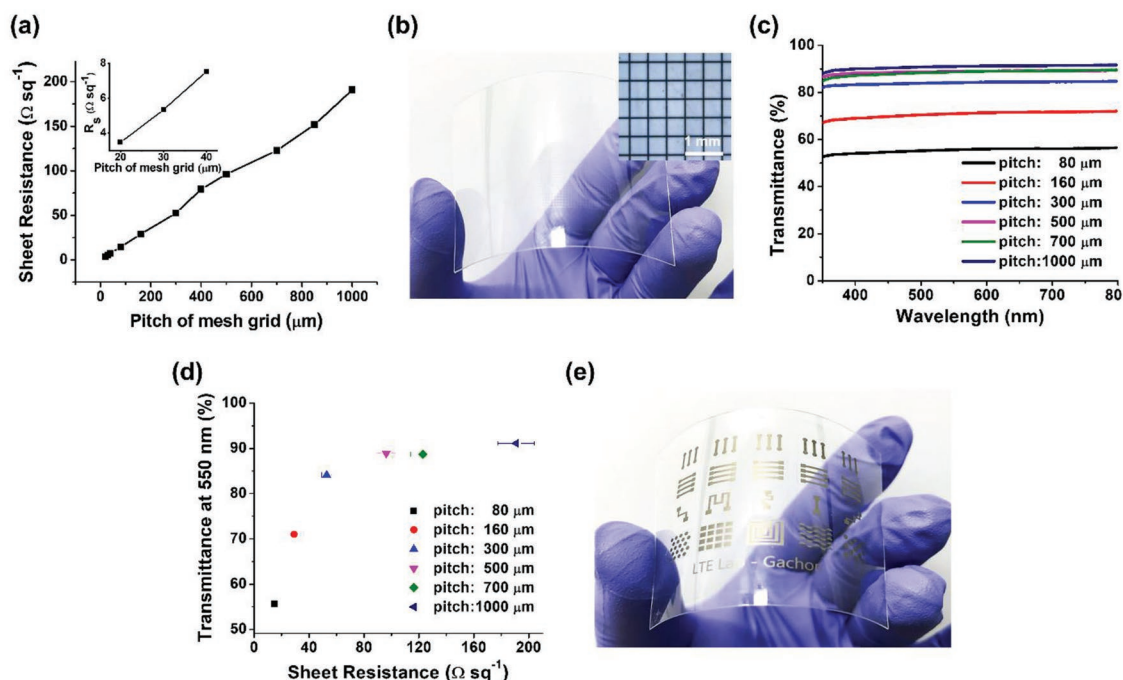
Figure 4. a) Sheet resistances at different grid sizes. The inset shows a magnified view in the grid size range of 20–40 µm. b) 3 cm × 3 cm mesh-type Ni electrodes with a pitch of 500 µm on PET. The inset shows an optical microscopy image. c) Substrate-based transmittance spectra of the mesh-type electrodes on PET with different pitches. d) Substrate-based transmittance as a function of the sheet resistance at different pitches. e) Customized Ni conductor patterns on a PET substrate.

change is negligible up to a bending radius of 10 mm even though resistance slightly increases after the bending cycle (inset of Figure 5a). The high electrical reliability is attributed to fully densified microstructure and robust adhesion of the electrodes to the substrate. In the convex mode, the relative resistance increases up to 2.84 at the bending radius of 10 mm possibly due to microfractures and crack generation. However, the resistance value is well retrieved after releasing from the convex bending even though the flat state resistance increases by 17% meaning that a small number of permanent discontinuities were formed in the electrodes. It is worth to note that the bending tests of the Ni electrodes were performed without any surface passivation. Figure 5b shows the change in relative resistance under various twisting angles. The degree of twisting is visualized in the inset figures. The behavior of the resistance change under twisting is similar to that of under bending. No noticeable resistance change is observed during the concave-mode twisting. The relative resistance increases up to 3.6 at the 360° convex-mode twisting, however, the flat state resistance increases only by 25% after releasing from the twisting. As shown in Figure 5c, the transparent mesh-type Ni pad on PET was used as a conductor in a circuit to connect a blue-light-emitting diode (LED) under an applied DC voltage of 3.5 V. There was no noticeable brightness change of the LED under both bending and twisting of the pad. To identify the long-term mechanical reliability of the Ni conductor pad, a cyclic bending test was performed; the experimental setup is shown in the inset of **Figure 5**d. Bending of the pad is created by moving one end at a frequency of 1 Hz on a motorized linear stage, while the other end is fixed, yielding a radius of curvature of r = 10 mm

at the maximum bending deformation. The resistance of the pad was measured at the flat state after every bending cycle. The resistance variation (R/R_o) is smaller than 3% after 10 000 bending cycles, as confirmed in Figure 5d. This superior bendability is attributed to the strong adhesion of the Ni electrodes onto the substrate and inherent resilience of the thin electrodes.

As a device demonstration of the mesh-type Ni conductor, a flexible transparent four-wire resistive touch screen panel (**Figure 6**a) was fabricated. The 2.5 cm × 4.5 cm mesh-type Ni grids with a pitch of 300 µm on the PET substrate (R_s: 52.8 Ω sq^{-1}, T: 84% at 550 nm) were fabricated as shown in Figure 6b. An ITO–PET film (R_s: 60 Ω sq^{-1}, T: 79% at 550 nm, Sigma-Aldrich) was used as a counter electrode. Two slips of copper tape were attached to the top and bottom sides of the Ni conductor while another two slips were attached to the left and right sides of the ITO–PET film; no additional protective coating layer was required for the Ni conductor owing to its strong adhesion to the substrate. The device was connected to a commercial USB-interface touch screen controller by which the voltage drop of a specific position on the panel is detected and converted to letters on a PC screen. The functionality of the touch screen panel is confirmed by writing the laboratory name

Table 1. Thermal properties of soda-lime glass and PET.

	Thermal conductivity, k [W m^{-1} K^{-1}]	Thermal diffusivity, α [m^2 s^{-1}]	$\alpha^{0.5}k^{-1}$
Soda-lime glass[15]	1.4	9.1×10^{-7}	6.8×10^{-4}
PET[16]	0.15	9.1×10^{-8}	2.0×10^{-3}

**ADVANCED
SCIENCE NEWS**

www.advancedsciencenews.com

**ADVANCED
FUNCTIONAL
MATERIALS**

www.afm-journal.de

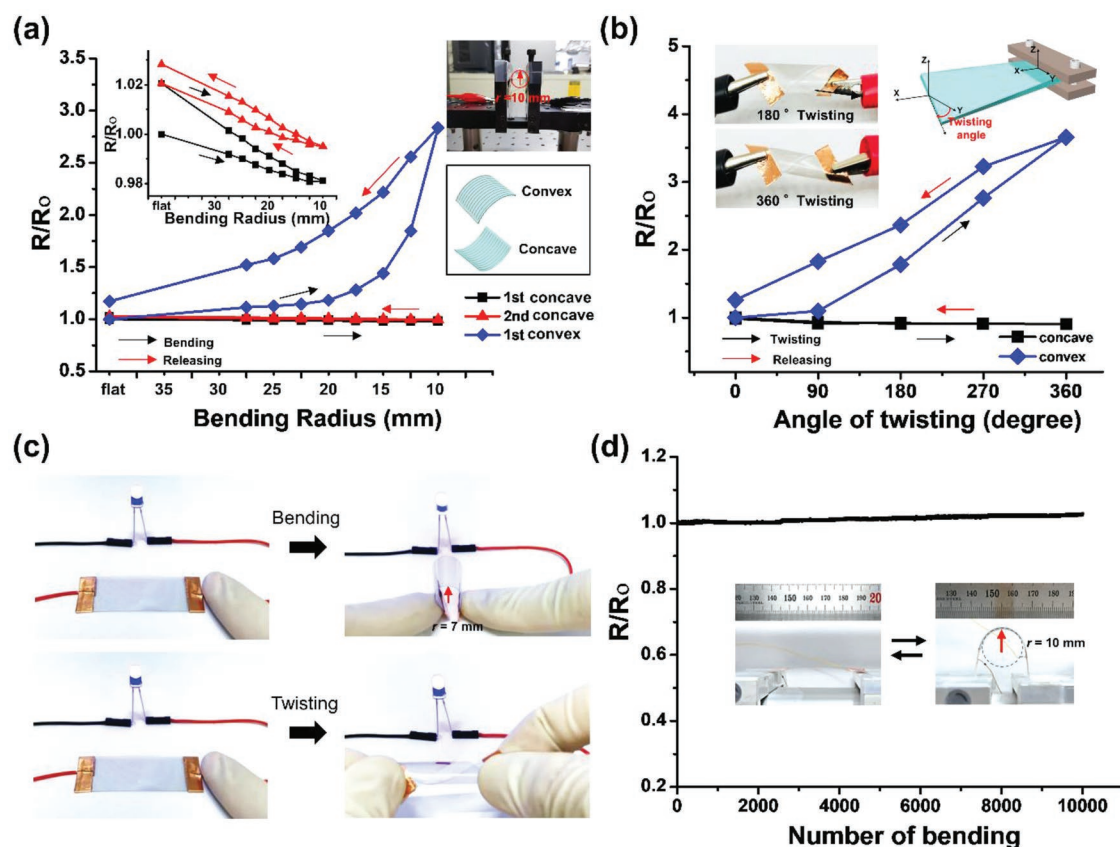**Figure 5.** Various mechanical and electrical performance tests of the 2.5 cm × 4.5 cm Ni conductor pad on PET. a) Relative resistance change at various bending radii. b) Relative resistance change under various twisting angles. c) Photographs of the glowing LED upon bending and twisting of the Ni transparent conducting panel in an electric circuit. d) Relative resistance change in the cyclic bending test (up to 10 000 cycles) with a bending radius of 10 mm.

on the device, as shown in Figure 6c. More details of assembling of the touch screen panel is provided in Section S10 in the Supporting Information, and touch screen demonstration on the curved surfaces having various curvatures is shown in Figure S11 and Movie S3 in the Supporting Information.

In order to demonstrate an additional application utilizing the high thermal stability of the Ni electrodes, the Ni conductors were applied to a flexible transparent heater. The heater composed of a 2.5 cm × 4.5 cm mesh-type Ni grid with a pitch of 300 μm (R_s: 52.8 Ω sq^{-1}, T: 84% at 550 nm) was prepared as illustrated in **Figure 7**a. A DC voltage was supplied to the thin-film heater through silver/copper contacts at the two ends. The temperature distribution of the heater was recorded using an infrared (IR) camera. Owing to the excellent thermal and electrical conductivities of the Ni electrodes as well as highly uniform surface of the Ni heater, a uniform temperature distribution was observed, as shown in Figure 7b. The temperature dependence of the heater on the applied voltage was measured in real-time by increasing the voltage stepwise from 3 to 11 V at intervals of 2 V every 2 min, as recorded in Figure 7c. The Ni heater exhibits a prompt temperature response upon the voltage alteration and rapid convergence to the plateau corresponding to the applied voltage. In order to avoid the permanent thermal deformation of the PET substrate, the applied voltage is limited to 11 V, at which the heater temperature is

approximately 83 °C. The performance repeatability of the heater was confirmed by switching the DC voltage repeatedly between 7 and 9 V at intervals of 2 min, as plotted in Figure 7d. Furthermore, the long-term heat-generation uniformity of the flexible transparent heater was verified by applying a constant voltage for 10 min, as shown in Figure 7e. The corresponding plateau temperatures for DC voltages of 5, 7, 9, and 11 V were 43, 56, 70, and 84 °C, respectively. As the PET substrate is bendable and lightweight, the fabricated Ni transparent heater, shown in Figure 7f, can be easily attached to a curved surface (diameter: 26 mm) of a glass vial with an excellent conformal coverage; a uniform heat performance is observed under the applied voltage. It is worth noting that the limiting factor of the highest heating temperature of the Ni flexible heater is not the oxidation temperature of the Ni electrode, but the glass-transition temperature of the substrate. As the Ni electrodes produced by this process can endure up to 400 °C, as mentioned above, the heater temperature can be increased as high as allowed by the substrate. The high thermal stability of the Ni electrodes was confirmed by fabricating a heater on a PI substrate, with a higher heat resistance. A 2.5 cm × 2.5 cm mesh-type Ni grid with a pitch of 300 μm was created on the PI substrate at a laser power of 22 mW and scanning speed of 50 mm s^{-1}. The flexible Ni heater on the PI substrate shown in Figure 7g achieves a uniform heat distribution at 280 °C under
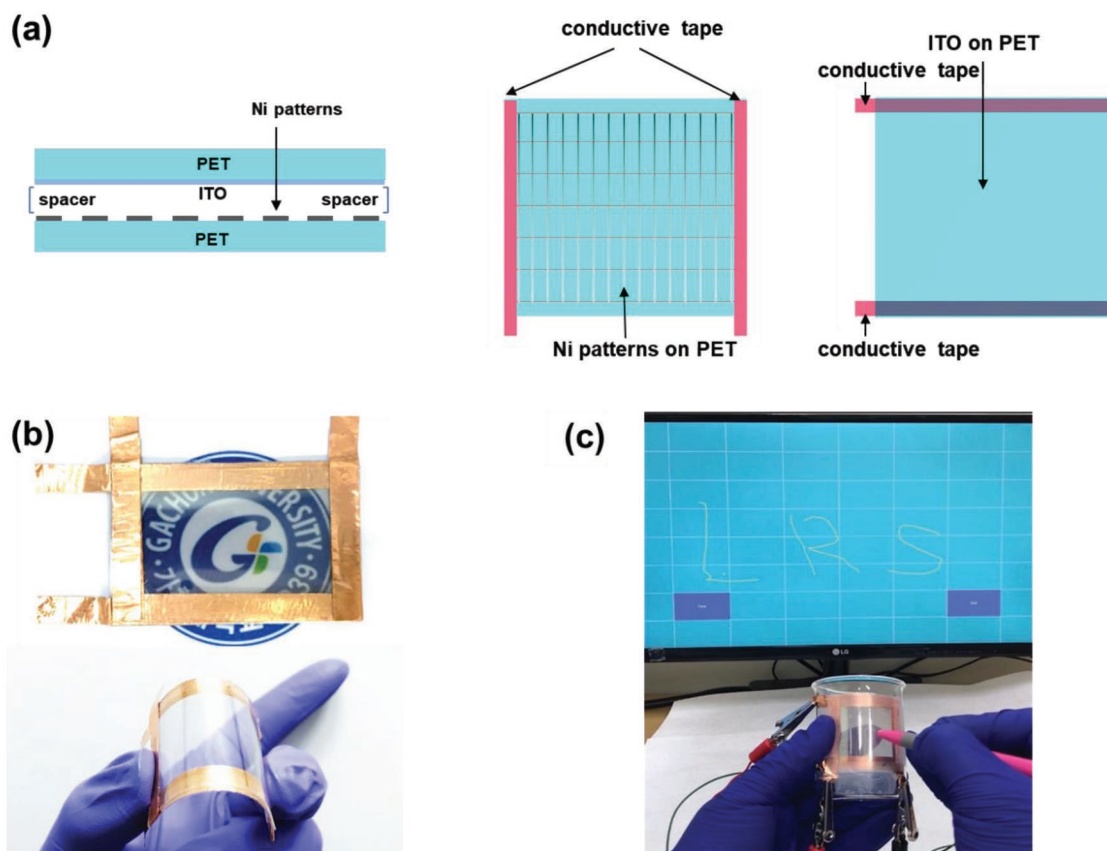
Figure 6. a) Schematic diagram of the touch screen panel using Ni conductors on a PET substrate. b) Photographs of the four-wire resistive touch screen panel at flat (top) and bending (bottom) states. c) Demonstration by writing the letters "LRS" on the flexible transparent touch screen attached on a curved surface.

a voltage of 30 V, which cannot be achieved with Cu electrodes owing to oxidation.

3. Conclusion

We developed a novel simple synthesis approach for large-scale production of NiO_x NP ink and laser digital patterning process to fabricate Ni-based flexible transparent conducting panels on various substrates through the LRS of solution-processed NiO_x thin films. The entire process, from material synthesis to subsequent LRS, was performed under ambient conditions, without conventional photolithographic procedures. Owing to substantially lowered applied laser power density for the reductive sintering of the reformulated NiO_x NPs, the Ni electrode patterning was successful even on the PET substrate. The resultant Ni conductors exhibited excellent thermal, chemical, and mechanical stabilities, confirmed by various measurement tests. The flexible mesh-type Ni conducting panels with a high transmittance and low sheet resistance ($T = 84\%$ at $R_s = 53 \ \Omega \ sq^{-1}$) were successfully applied for touch screen panels and high-performance transparent electrical heaters. These results will pave the way for the use of versatile, flexible, and transparent Ni electrodes, which can substitute conventional materials such as Ag, Cu, and ITO.

4. Experimental Section

NiO_x NP Ink Synthesis: The NiO_x NPs were synthesized by calcination of $Ni(OH)_2$ produced by a chemical precipitation method with considerable quantitative variations, compared with the previous study.[17] Nickel(II) nitrate hexahydrate $Ni(NO_3)_2 \cdot 6H_2O$, sodium hydroxide NaOH, and CTAB were purchased from Alfa Aesar. Polyvinylpyrrolidone (PVP, $M_w \approx 10\ 000$) was purchased from Sigma-Aldrich. All reagents were used without further purification. 2.5 mol of $Ni(NO_3)_2 \cdot 6H_2O$ was dissolved in 500 mL DI water. Then, NaOH solution (10 M) was added into the solution drop by drop until the pH value reached 10 to produce $Ni(OH)_2$ colloid suspension. The pH value change corresponding to the amount of the added NaOH solution is plotted in Figure S12 in the Supporting information. The colloidal $Ni(OH)_2$ was centrifuged at 3000 rpm for 5 min, washed with DI water several times, and then dried at 80 °C for 6 h. The $Ni(OH)_2$ powder was baked at 270 °C for 2 h in a convection oven to produce dark-black nonstoichiometric NiO_x NPs by the following reaction:[17]

$$Ni(OH)_2 \rightarrow NiO_x + H_2O$$
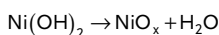
NiO_x NP ink was prepared by dispersing NiO_x (31 wt%) NPs, PVP (6.8 wt%), and CTAB (0.5 wt%) into 1-pentanol (61.7 wt%). The mixture is then ultrasonicated for 20 h to produce well-dispersed NP ink.

NiO_x NP Thin Film Deposition: Soda lime glass, PET, and PI were used as the substrates. After regular cleaning process, oxygen plasma was applied on them to enhance the adhesion between the NP ink and the
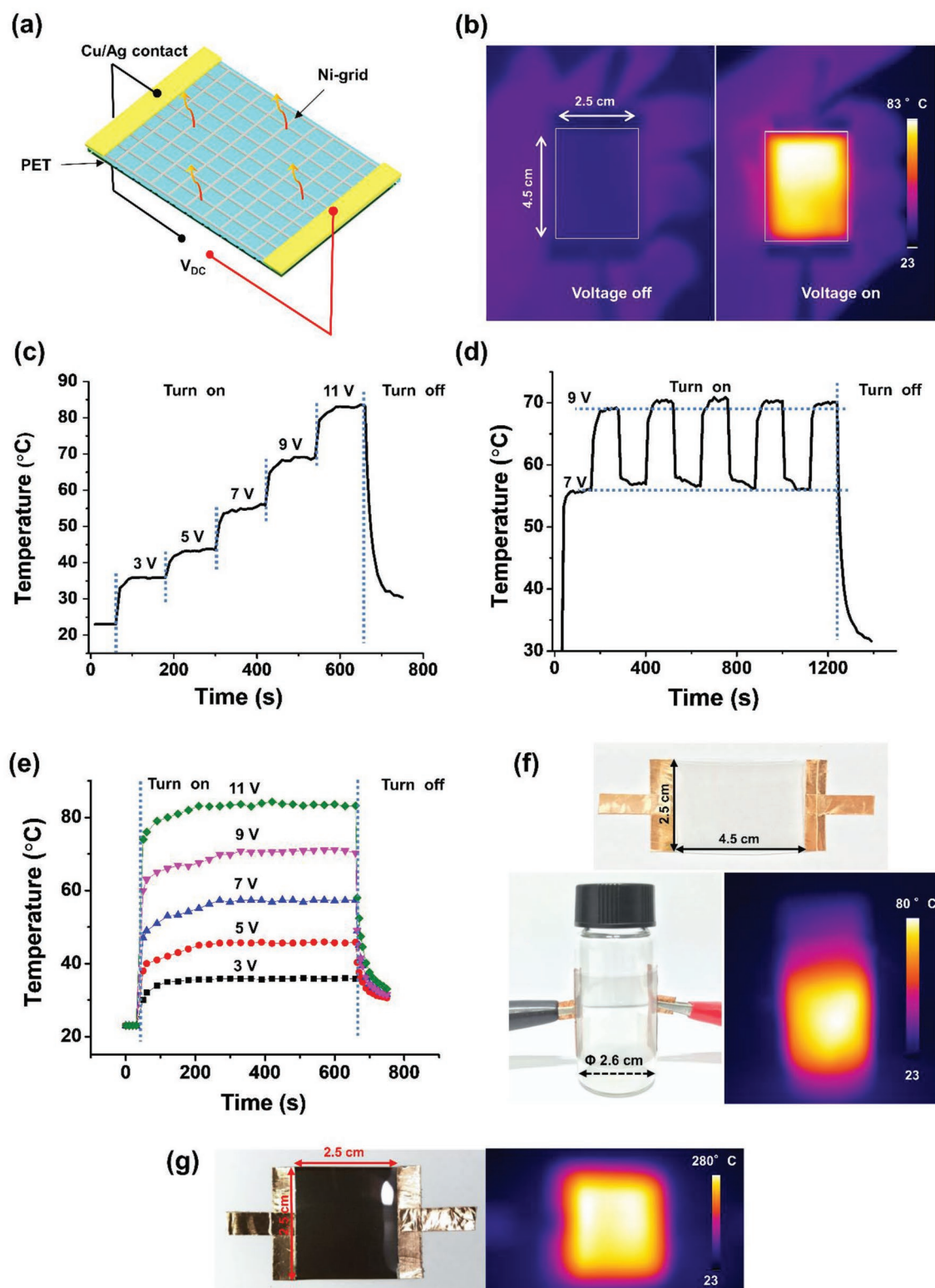
Figure 7. a) Schematic structure of a flexible transparent Ni-grid heater. b) IR images of Ni-grid heater on PET at an initial state (left) and at a voltage-applied state (right). c) Change in temperature as a function of time for incrementally increased applied biases. d) Cyclic performance of the heater under repetitive applying 7 and 9 V. e) The long-term heat-generation uniformity of the flexible transparent heater verified by applying each constant voltage for 10 min. f) Photographs of a transparent Ni-grid heater on PET (top), the heater under bending condition (left) by wrapping around the 26 mm diameter glass vial, and its IR image at heated state (right). g) Photograph of a flexible Ni-grid heater on PI and its IR images at a voltage applied state.

**ADVANCED
SCIENCE NEWS**
www.advancedsciencenews.com

**ADVANCED
FUNCTIONAL
MATERIALS**
www.afm-journal.de

substrates. NiO$_x$ thin films on every substrate were deposited by spin coating at 1000 rpm for 60 s in this study. It was noted that the desired thin film thickness could be altered by adjusting the concentration of NiO$_x$ ink and spin speed.

CuO$_x$ NP Ink Synthesis and CuO$_x$ NP Thin Film Deposition: CuO$_x$ NPs were synthesized in a same way as the NiO$_x$ except substituting Cu(NO$_3$)$_2$·3H$_2$O for Ni(NO$_3$)$_2$·6H$_2$O. After baking Cu(OH)$_2$ powder, dark-brown non-stoichiometric CuO$_x$ NPs were produced by the following reaction.

$$Cu(OH)_2 \rightarrow CuO_x + H_2O$$
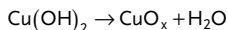
CuO$_x$ ink was prepared by dispersing CuO$_x$ NP with PVP and CTAB in 1-pentanol with the same formulation. For the corrosion test, a 2 cm × 0.5 cm Cu electrodes was fabricated by the LRS process.

LRS Process: A 532 nm CW laser beam was controlled by a galvanometer scanner (HurrySCAN III, Scanlab) integrated with a CAD system (laserDESK, Scanlab).

Materials Characterization: The size and crystal structure of the synthesized NiO$_x$ NPs were measured by TEM (JEOL JEM-2100F). The surface morphology was characterized using SEM (Hitachi S-4800) and AFM (Park System XE100). EDS analysis was conducted to investigate the elemental mapping images. The transmittance data was measured using a spectrophotometer (Varian-Cary 5000). The power supply (Gwinstek, GPS-4303) was used to apply DC voltage to the devices, and temperature distribution was measured using an IR camera (Testo 872).

Supporting Information

Supporting Information is available from the Wiley Online Library or from the author.

Conflict of Interest

The authors declare no conflict of interest.

[1] a) J. Song, H. Zeng, *Angew. Chem., Int. Ed.* **2015**, *54*, 9760; b) J. Song, J. Li, J. Xu, H. Zeng, *Nano Lett.* **2014**, *14*, 6298; c) Y. D. Suh, J. Kwon, J. Lee, H. Lee, S. Jeong, D. Kim, H. Cho, J. Yeo, S. H. Ko, *Adv. Electron. Mater.* **2016**, *2*, 1600277; d) J. H. Park, G. T. Hwang, S. Kim, J. Seo, H. J. Park, K. Yu, T. S. Kim, K. J. Lee, *Adv. Mater.* **2017**, *29*, 1603473.

[2] a) J. Yeo, S. Hong, D. Lee, N. Hotz, M. T. Lee, C. P. Grigoropoulos, S. H. Ko, *PLoS One* **2012**, *7*, e42315; b) J. B. In, D. Lee, F. Fornasiero, A. Noy, C. P. Grigoropoulos, *ACS Nano* **2012**, *6*, 7858; c) S. H. Ko, H. Pan, D. Lee, C. P. Grigoropoulos, H. K. Park, *Jpn. J. Appl. Phys.* **2010**, *49*, 05EC03; d) M. T. Lee, D. Lee, A. Sherry, C. P. Grigoropoulos, *J. Micromech. Microeng.* **2011**, *21*, 095018; e) H. Kwon, W. Choi, D. Lee, Y. Lee, J. Kwon, B. Yoo, C. P. Grigoropoulos, S. Kim, *Nano. Res.* **2014**, *7*, 1137; f) W. Shou, B. K. Mahajan, B. Ludwig, X. Yu, J. Staggs, X. Huang, H. Pan, *Adv. Mater.* **2017**, *29*, 1700172.

[3] a) S. Hong, J. Yeo, G. Kim, D. Kim, H. Lee, J. Kwon, H. Lee, P. Lee, S. H. Ko, *ACS Nano* **2013**, *7*, 5024; b) S. H. Ko, H. Pan, C. P. Grigoropoulos, C. K. Luscombe, J. M. Fréchet, D. Poulikakos, *Nanotechnology* **2007**, *18*, 345202; c) I. Theodorakos, F. Zacharatos, R. Geremia, D. Karnakis, I. Zergioti, *Appl. Surf. Sci.* **2015**, *336*, 157; d) M. Bashouti, A. Manshina, A. Povolotckaia, A. Povolotskiy, A. Kireev, Y. Petrov, M. Mačković, E. Spiecker, I. Koshevoy, S. Tunik, *Lab Chip* **2015**, *15*, 1742.

[4] a) B. Kang, S. Han, J. Kim, S. Ko, M. Yang, *J. Phys. Chem. C* **2011**, *115*, 23664; b) M. Mizoshiri, S. Arakane, J. Sakurai, S. Hata, *Appl. Phys. Express* **2016**, *9*, 036701; c) S. Han, S. Hong, J. Ham, J. Yeo, J. Lee, B. Kang, P. Lee, J. Kwon, S. S. Lee, M. Y. Yang, *Adv. Mater.* **2014**, *26*, 5808; d) S. Han, S. Hong, J. Yeo, D. Kim, B. Kang, M. Y. Yang, S. H. Ko, *Adv. Mater.* **2015**, *27*, 6397; e) V. B. Nam, D. Lee, *Nanomaterials-Basel* **2016**, *6*, 47.

[5] a) Z. Han, F. Qiu, R. Eisenberg, P. L. Holland, T. D. Krauss, *Science* **2012**, *338*, 1321; b) P. A. Nelson, J. M. Elliott, G. S. Attard, J. R. Owen, *Chem. Mater.* **2002**, *14*, 524.

[6] C. Gu, J. Lian, J. He, Z. Jiang, Q. Jiang, *Surf. Coat. Technol.* **2006**, *200*, 5413.

[7] a) Y. Jo, S.-J. Oh, S. S. Lee, Y.-H. Seo, B.-H. Ryu, D. H. Yoon, Y. Choi, S. Jeong, *J. Mater. Chem. C* **2015**, *3*, 4842; b) C. Chinnasamy, B. Jeyadevan, K. Shinoda, K. Tohji, A. Narayanasamy, K. Sato, S. Hisano, *J. Appl. Phys.* **2005**, *97*, 10J309; c) Y. Chen, D.-L. Peng, D. Lin, X. Luo, *Nanotechnology* **2007**, *18*, 505703.

[8] a) D. Paeng, D. Lee, J. Yeo, J.-H. Yoo, F. I. Allen, E. Kim, H. So, H. K. Park, A. M. Minor, C. P. Grigoropoulos, *J. Phys. Chem. C* **2015**, *119*, 6363; b) D. Lee, D. Paeng, H. K. Park, C. P. Grigoropoulos, *ACS Nano* **2014**, *8*, 9807.

[9] Y. Rho, K.-T. Kang, D. Lee, *Nanoscale* **2016**, *8*, 8976.

[10] a) H.-J. Hwang, W.-H. Chung, H.-S. Kim, *Nanotechnology* **2012**, *23*, 485205; b) J. Ryu, H.-S. Kim, H. T. Hahn, *J. Electron. Mater.* **2011**, *40*, 42.

[11] K. Woo, Y. Kim, B. Lee, J. Kim, J. Moon, *ACS Appl. Mater. Interfaces* **2011**, *3*, 2377.

[12] H. Lee, M. Yang, *Appl. Phys. A: Mater.* **2015**, *119*, 317.

[13] J. Van De Groep, P. Spinelli, A. Polman, *Nano Lett.* **2012**, *12*, 3138.

[14] J. Kwon, H. Cho, H. Eom, H. Lee, Y. D. Suh, H. Moon, J. Shin, S. Hong, S. H. Ko, *ACS Appl. Mater. Interfaces* **2016**, *8*, 11575.

[15] T. L. Bergman, A. S. Lavine, F. P. Incropera, D. P. Dewitt, *Fundamentals of Heat and Mass Transfer*, John Wiley Sons, New York **2011**.

[16] J. G. Speight, *Lange's Handbook of Chemistry*, McGraw-Hill, New York **2005**.

[17] F. Jiang, W. C. Choy, X. Li, D. Zhang, J. Cheng, *Adv. Mater.* **2015**, *27*, 2930.